Article

Temperature Characteristics of Axle-Box Bearings Under Wheel Flat Excitation

Yaping Luo [1], Fan Zhang [2],*, Zhiwei Wang [1], Chen Yang [1], Weihua Zhang [1] and Fengshou Gu [3]

[1] State Key Laboratory of Rail Transit Vehicle System, Southwest Jiaotong University, Chengdu 610031, China
[2] School of Design, Southwest Jiaotong University, Chengdu 610031, China
[3] Centre for Efficiency and Performance Engineering, University of Huddersfield, Huddersfield HD1 3DH, UK
* Correspondence: fan.zhang@swjtu.edu.cn

Abstract: The high-amplitude and high-frequency wheel–rail impacts excited by wheel flat result in severe contact friction in axle-box bearing (ABB), and the friction can cause a temperature rise or even structural damage of ABB. To this end, a thermal analysis model considering the vehicle operation environment is proposed to analyze the temperature characteristics of ABB. Various coupling dynamics effects between the vehicle–track system and ABB are synergistically integrated. The heat conduction, convection, and radiation between the various components of ABB are also integrated into the thermal analysis modeling. By the field tests, the accuracy of the ABB thermal model is validated. The results obtained through the model simulation show that the ABB temperature increases with vehicle speed and wheel flat length, and the ABB temperature at the outside row is higher than that at the inside row. Moreover, the temperature of the roller, cage, inner ring, outer ring, and axle box increases following an ascending order. Specifically, the temperature at the small end of the roller is higher than that at the large end. The findings of this study can provide engineering guidelines for the condition monitoring of ABBs.

Keywords: axle-box bearing; temperature characteristic; wheel flat; thermal analysis model; vehicle operation environment

1. Introduction

Axle-box bearing (ABB) is a core component of a train bogie, and its temperature often increases rapidly in a short time when it works under abnormal states, leading to hot-axle or even cutting-axle accidents and threatening train safety in severe cases. Therefore, ABB temperature is a key monitoring factor of train online monitoring systems [1]. Usually, ABB directly withstands high-amplitude and high-frequency wheel–rail impacts originated from the wheelset. Wheel flat, as an inevitable phenomenon in vehicle service, can result in an obvious increase in wheel–rail impact [2], which can induce violent friction inside ABB; subsequently, excessive frictional heat is generated. When ABB rotates at high speed, frictional heat cannot spread to the surrounding environment in time, causing the abnormal temperature rise [3]. This situation accelerates bearing wear, shortens its service life [4,5], and even causes early scrapping. Hence, investigating the temperature characteristics of ABB excited by wheel flat is crucial for bearing condition monitoring and maintenance as well as the safety of train operation.

The temperature characteristics of ABB are affected by internal factors and external excitation. Previous studies have mainly focused on internal factors, e.g., structural parameters, part assembly relationships, heat generation, and heat transfer performances. Regarding the structural parameters of ABB, Wang et al. [6] conducted a thermal–mechanical

analysis of railway axles with tapered roller bearings to study the influence of initial radial clearance between the taper and axle on ABB temperature. Based on generalized Ohm's law, Ai et al. [7] built an ABB thermal network model to analyze the bearing's temperature against different roller large-end spherical radii. For the assembly relationship of bearing components, Li et al. [8] analyzed the influence of the tilting outer ring on the bearing friction heat. As a result, the larger the tilting angle of the outer ring is, the higher its steady-state temperature is. Considering that the temperature changes caused by heat generation and transfer factors are also crucial, Yan et al. [9] developed a heat generation model that combined the elastohydrodynamic lubrication theory to investigate the thermal generation performances of the ABB in terms of structural parameters. The results show that the heat generated by the raceway was significantly greater than that of the other parts. Tarawneh et al. [10,11] quantified the path of heat transfer inside ABBs through a series of tests and theoretical research to explain the various mechanisms leading to overheating and analyzed the overheating problem of railway bearings using the finite element method (FEM) [12].

However, the thermal characteristics of ABBs are not only related to the bearing itself but also remarkably related to the load on the bearing due to external excitation. Recently, researchers investigated the effect of the service environment on ABB temperature. Vladimir et al. [13] constructed the thermal model for railway cylindrical bearings to study ABB temperatures on linear and curved railways as well as different curve radii and heights, which all induce an ABB temperature increase. In addition, Vladimir compared the temperatures of railway cylindrical bearings at different vehicle speeds. Recently, Zhou et al. [14] and Gao et al. [15] analyzed the influence of vehicle speed on the temperature of railway tapered bearings using a thermal analysis test platform and FEM, respectively. The results show that ABB temperature increases with speed and regardless of the shape of the bearings (e.g., cylindrical or tapered bearings). Considering the effect of vibration environments of ABBs on high-speed vehicles, Wang et al. [16] calculated the dynamic and temperature characteristics of ABBs at different positions for two vehicle types; they found that the traction drive system has a certain impact on ABB temperature. In summary, external excitation imposes an additional load on ABBs, contributing to their temperature increase.

Previous studies have mainly focused on the effects of railway lines and vehicle speeds on the thermal characteristics of ABBs. However, ABB is directly connected with the wheelset; the effect of wheel–rail impact on ABB temperature cannot be ignored. Particularly, under wheel flat excitation, the wheel–rail impact is strengthened. This significantly affects the service safety of ABB and even the entire vehicle. Thus, it is crucial to investigate the ABB thermal characteristics impacted by wheel flat.

In this work, we propose an ABB thermal model coupling the vehicle operation environment. This model integrates the influence of various internal factors: lubrication status, heat generation, heat transfer, etc. With the proposed model, the temperature characteristics of ABBs under the external excitation, including wheel flat defects and driving speed, are revealed to analyze the heat transfer laws of each ABB component. Following this, local failure areas due to an excessive temperature increase are analyzed to guide the structural design, condition monitoring, and real-time maintenance of ABBs.

2. ABB Thermal Model Coupling Vehicle Operation Environment

The modeling process of the proposed thermal model of the ABB is shown in Figure 1, including two parts: (1) vehicle operation environment modeling and (2) thermal analysis modeling.
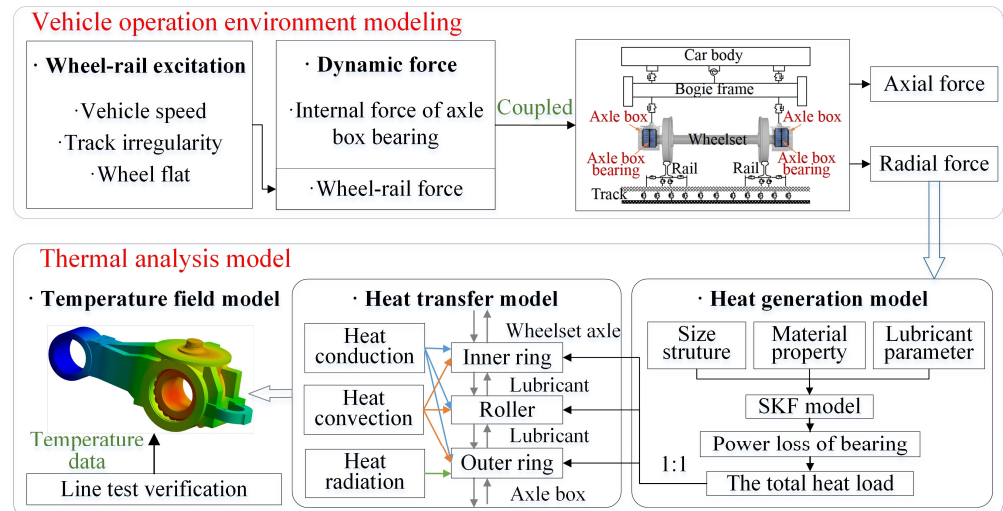
Figure 1. Overall modeling process.

Vehicle operation environment modeling: a rigid–flexible coupled vehicle dynamic model, which integrates flexible axle boxes, is established [17]. Next, the ABB internal force is coupled into the vehicle system. Further, the dynamics coupling between track and vehicle systems is realized via the wheel–rail force, which considers the impact of track irregularity and the excitation of wheel flat. Based on this, dynamics forces along the radial and axial directions inside ABBs excited by the wheel flat are obtained. These serve as inputs for the thermal analysis model.

Thermal analysis modeling: based on the dynamic forces, the thermal analysis model of ABB is established. First, the bearing friction moment is calculated to obtain the power loss using the SKF model [18]. Next, the friction heat generated by the power loss is evenly distributed on the contact surface between the bearing rollers and rings. During heat transfer, heat conduction, convection, and radiation are synthetically considered. Subsequently, a three-dimensional temperature field model of ABB is developed using FEM. Moreover, online tests and simulations are conducted to validate the proposed model.

2.1. Dynamic Boundary of ABB

2.1.1. Vehicle–Track Coupled Dynamics Model with Wheel Flat

The built vehicle–track coupled dynamics model is depicted in Figure 2. In the vehicle system, ABBs are installed in the axle boxes, which are affected by external excitations comprising wheelset impacts, car body load, and bogie frame load. Additionally, flexible bodies, e.g., axle boxes, are developed using the modal superposition method [19,20]. For more detailed information on vehicle dynamics modeling, please refer to our previous work [17].

For the track system, the classic slab-track structure [21,22], which comprises rails and slabs, is considered. Track irregularity can excite the ABB via the wheel–rail contact. The normal wheel–rail force [23,24] mainly depends on the relative displacement $\delta Z_{wr}(t)$ at the contact position [25]. $\delta Z_{wr}(t)$ is given by

$$\delta Z_{wr}(t) = Z_w(t) - Z_r(x_w, t) - Z_t(t) - r(t), \tag{1}$$

where $Z_w(t)$ and $Z_r(x_w, t)$ denote displacements of the wheelset and rail along the radial direction, and $Z_0(t)$ denotes the vertical irregularity of the track. In the existence of the

wheel flat defect (Figure 3a), the variation in the wheel radius $r(t)$ with the flat depth D_f and flat length L_f is as follows [26]:

$$r(t) = \frac{1}{2}D_f\left[1 - \cos\left(2\pi x/L_f\right)\right], \tag{2}$$

where $D_f = L_f^2/(16\,R)$; R denotes the wheel nominal radius. Based on Formula (2), the $r(t)$ with respect to L_f is plotted in Figure 3b.
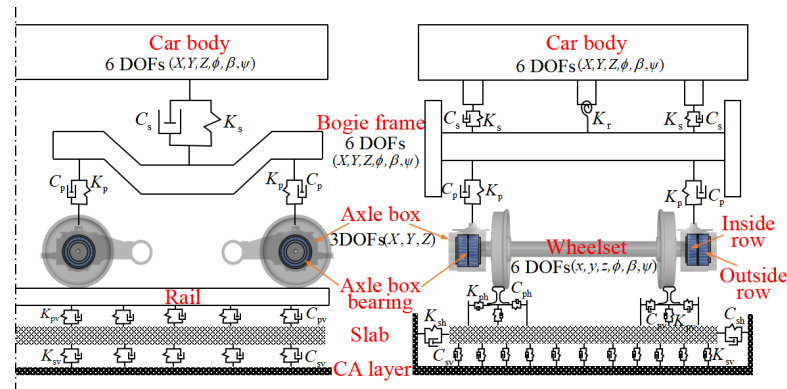

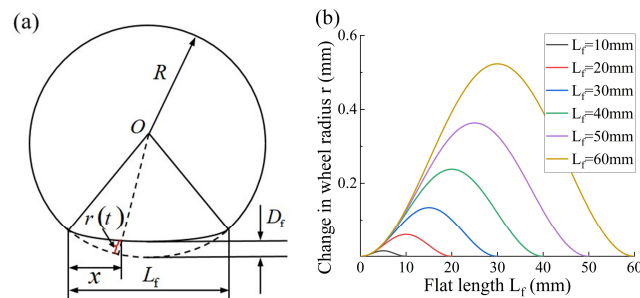**Figure 2.** Rigid–flexible coupled dynamics model of high-speed train.

Figure 3. (**a**) Geometric model of wheel flat and (**b**) change in wheel radius with L_f.

2.1.2. Internal ABB Force

In addition to external loads, ABBs are subjected to internal excitation induced by nonlinear contact inside the bearing. The geometric structure and dynamics model of the ABB are shown in Figure 4.
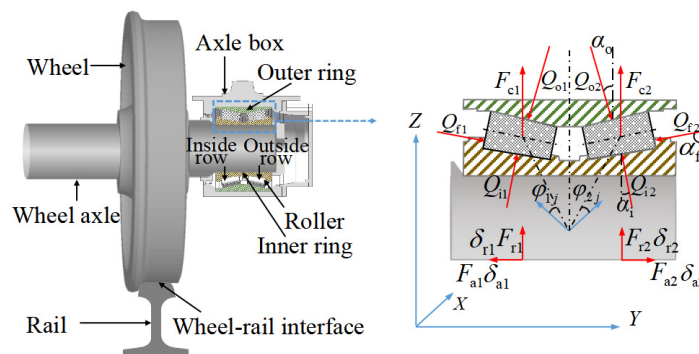

Figure 4. Dynamics model of ABB.

In the ABB dynamics model, considering the longitudinal, lateral, and vertical motions, the dynamic force Q_{omj} between the roller j and the raceway of the outer ring is determined by the relative displacement δ_{omj} and contact stiffness K_o between the two [27,28].

$$Q_{omj} = \begin{cases} K_o \delta_{omj}^{10/9}, \delta_{omj} > 0 \\ 0 \quad , \delta_{omj} < 0 \end{cases} \quad m = 1, 2 \quad j = 1{-}21, \tag{3}$$

To this end, the radial force F_{rm} and axial force F_{am} of the bearing can be obtained:

$$\begin{array}{l} F_{rm} = \sum_{j=1}^{21} Q_{omj} cos\alpha_o cos\phi_{mj} + C_a \left(\dot{X}_a - \dot{X}_w \pm d_w \dot{\psi}_w \right), \ m = 1, 2 \ j = 1{-}21 \\ F_{am} = \sum_{j=1}^{21} Q_{omj} sin\alpha_o + C_a \left(\dot{Y}_a - \dot{Y}_w \right) \end{array} \tag{4}$$

where subscripts a and w, respectively, represent the axle box and wheelset; C_a denotes the bearing damping coefficient; X and Y denote the displacements along the longitudinal and lateral directions; and ψ_w and ϕ_w denote the yaw and roll motions. d_w denotes the semi-lateral distance between primary suspensions. These forces act on the axle box and wheelset simultaneously, realizing dynamic coupling between ABB and the vehicle system.

Utilizing the constructed vehicle–track dynamics model integrating bearings, the dynamic load (axial force and radial force) of the ABB under wheel flat excitation can be solved, referring to the previous report [17]. This solved bearing load is used as the dynamic boundary for the thermal analysis model. Then, the impact of the bearing load induced by wheel flat on ABB temperature and heat distribution can be further calculated.

2.2. Thermal Analysis Model of ABB

The FEM model is developed based on the parameters of ABB employed in high-speed trains [16]. The model is meshed by a hexahedral grid using HyperMesh software (Figure 5a), in which the roller contact areas are refined to ensure calculation accuracy. Subsequently, the meshed model is imported into Ansys Workbench software. Within this software, heat sources are applied (Figure 5b) and heat transfer parameters (Figure 5c,d) are set. Thus, the thermal analysis model of ABB is established. Heat is transferred between bearing components via conduction, convection, and radiation to reach thermal equilibrium. The details of the heat generation and transfer are presented as follows.
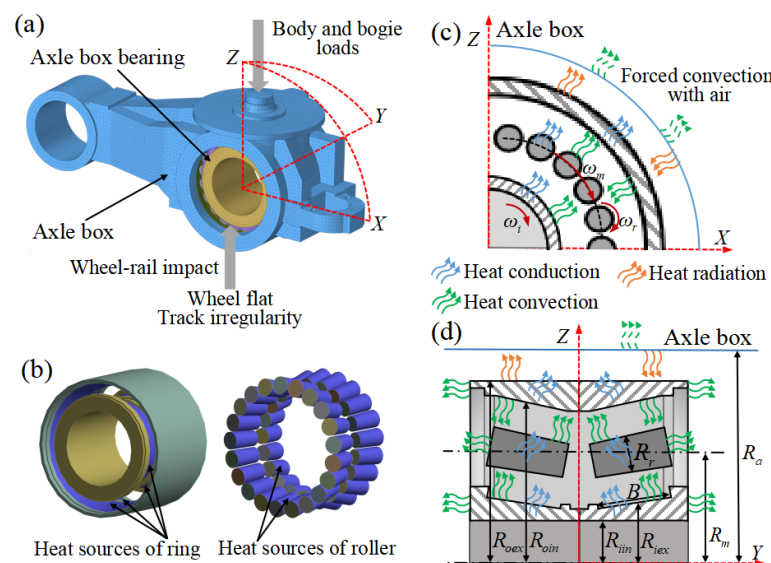

Figure 5. Thermal analysis model: (**a**) FEM, (**b**) heat source distribution, and (**c,d**) heat transfer model of ABB.

2.2.1. Heat Generation Model

1. Power loss of ABB:

The friction power loss P of ABB can be calculated with friction moment M. Following the SKF model [18,29], M comprises the rolling friction moment, M_{rr}; sliding friction moment, M_{sl}; friction moment of the seals, M_{seal}; and friction moment of drag losses, churning, and splashing, M_{drag}.

$$P = M\left(\frac{V}{3.6R}\right), \tag{5}$$

$$M = M_{rr} + M_{sl} + M_{seal} + M_{drag}, \tag{6}$$

where V denotes the vehicle speed.

In this work, M_{rr} is rewritten with the inlet shear heating reduction factor ϕ_{ish} and kinematic replenishment/starvation reduction factor ϕ_{rs} [30]:

$$M_{rr} = \phi_{ish}\phi_{rs}G_{rr}(v_l n_b)^{0.6}, \tag{7}$$

$$\phi_{ish} = \left[1 + 1.84 \times 10^{-9}(2n_b R_m)^{1.28}v_l^{0.64}\right]^{-1}, \tag{8}$$

$$\phi_{rs} = \exp\left(-2k_{rs}v_l n_b(R_{iex} + R_{oin})\sqrt{k_z/4(R_{oin} - R_{iex})}\right), \tag{9}$$

where k_{rs} denotes the replenishment/starvation constant; k_z denotes the geometry constant related to the bearing type; R_m denotes the ABB pitch radius; R_{iex} and R_{oin}, respectively, denote the external radius of the inner ring and the internal radius of the outer ring; n_b denotes the ABB rotational speed; and v_l denotes the kinematic viscosity of the lubricant. G_{rr} denotes the rolling friction parameter, which depends on the bearing structure and internal force [31], and its calculation formula is

$$G_{rr} = R_1(2R_m)^{2.38}(F_r + R_2\gamma_b F_a)^{0.31}, \tag{10}$$

where R_1 and R_2 are geometrical constants; γ_b is the axial load factor, determined by the average of axial load and radial load [32]:

$$\begin{cases} F_{am}/F_{rm} \leq e \rightarrow \gamma_b = 1.6 \\ F_{am}/F_{rm} > e \rightarrow \gamma_b = 2.3 \end{cases}, \tag{11}$$

where e is the assumed parameter; $e = 0.43$ for tapered roller bearing.

Moreover, M_{sl}, which is the slipping friction moment, is given by

$$M_{sl} = G_{sl}\mu_{sl}, \tag{12}$$

$$\mu_{sl} = \phi_{bl}\mu_{bl} + (1 - \phi_{bl})\mu_{EHL}, \tag{13}$$

$$\phi_{bl} = \exp\left(-5.2 \times 10^{-8}(n_b v_l)^{1.4}R_m\right), \tag{14}$$

where μ_{bl} and μ_{EHL} are constants that depend on the lubricant and friction coefficient in the full film condition, respectively ($\mu_{bl} = 0.15$ and $\mu_{EHL} = 0.05$) [33], and ϕ_{bl} denotes the mixed lubrication weighting factor [34]. G_{sl} denotes the sliding friction parameter [35], calculated by

$$G_{sl} = S_1(2R_m)^{0.82}(F_r + S_2\gamma_b F_a), \tag{15}$$

where S_1 and S_2 are geometrical constants.

In addition, the frictional torque from integral seals, M_{seal}, is calculated from the following [32]:

$$M_{seal} = K_{S1}d_s^{\beta} + K_{S2},\tag{16}$$

where d_s is the seal diameter; K_{S1}, K_{S2}, and β are constants assumed for tapered roller bearing.

In this study, M_{drag} is ignored because ABBs are lubricated with grease, generating negligible drag losses.

2.   Heat source distribution:

When the vehicle is in operation, the wheelset drives the ABB to rotate at high speed. As illustrated in Figure 6, the roller contacts the raceway of the outer ring at position i at time t_i; after a shorter period, $t_{i+1} - t_i$, the contact area quickly moves to position $i + 1$. Similarly, the contact area between the roller and the raceway of the inner ring moves accordingly. Therefore, each roller can serve as a heat source, concurrently heating the inner and outer rings. The heat load Q at the contact area A is expressed as follows [36]:

$$Q = \frac{P}{A} \times I,\tag{17}$$

where I denotes the heat distribution coefficient [37]. For ABB, the heat source is allocated between the rollers and ring raceway in a 1:1 ratio (Figure 5b).
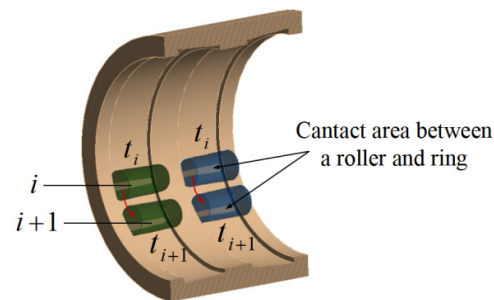

Figure 6. A schematic illustration of contact between the roller and the raceway of the outer ring.

2.2.2. Heat Transfer Model

1.   Heat conduction:

Inside the ABB, heat is conducted within each component. The inner and outer rings can be regarded as circular annular structures. For the inner ring, the heat conduction [38] is expressed as follows:

$$H_{ic} = \frac{2\pi k_b B_i}{\ln(R_{iex}/R_{iin})}(T_{iin} - T_{iex}),\tag{18}$$

where B_i denotes the inner ring width, k_b denotes the thermal conductivity of the bearing material, R_{iin} denotes the internal radius of the inner ring, and T_{iin} and T_{iex} denote the temperatures at the internal and external surfaces of the inner ring, respectively. The heat conduction within the outer ring is similar to that of the inner ring.

The heat conduction within the roller is expressed as follows:

$$Q_{rc} = \frac{\pi k_b l_r}{D_r}(T_1 - T_2),\tag{19}$$

where T_1 and T_2 are the temperatures of two points; D_r is the roller diameter.

2. Heat convection:

Heat convection occurs between the lubricants and the surfaces of the solid ABB components. Thus, the forced heat convection between the rotating inner ring surface and the lubricant is considered, and its coefficient can be calculated as follows [39]:

$$h_i = 0.19 \frac{k_l}{2R_{iex}} \left(Re_{Di}^2 + Gr_{Di} \right), \tag{20}$$

$$Re_{Di} = \frac{\omega_i (2R_{iex})^2}{v_l}, \tag{21}$$

$$Gr_{Di} = \frac{Bg(T_{iex} - T_\infty)(2R_{iex})^2}{v_l^2}, \tag{22}$$

where k_l denotes the thermal conductivity of the lubricant; Re and Gr denote the Reynolds and Grashov numbers, respectively; and ω_i denotes the angular velocity of the inner ring. B denotes the volume expansion coefficient of the lubricant, and g is the gravity acceleration. The specific parameters of the ABB lubricant described in reference [7] are identical to those in this text.

Similarly to the inner ring, the forced heat convection between the rotating roller surface and lubricant is considered, and its coefficient is given by

$$h_r = 0.33 \frac{k_l}{D_r} \left(\frac{\omega_r D_r}{v_l} \right)^{0.57}, \tag{23}$$

where ω_r denotes the angular velocity of the roller.

Meanwhile, due to the outer ring being fixed, it does not rotate with ABB. The heat transfer between the internal surface of the outer ring and the lubricant is realized by natural convection; therefore, its coefficient is given by the following [15]:

$$h_o = 0.53 \frac{k_l}{2R_{oin}} (Gr_{Do} Pr_{Do})^{0.25}, \tag{24}$$

The forced heat convection between the external surface of the axle box and ambient air is considered during forward vehicle movement, and its coefficient is given by

$$h_a = 0.03 \frac{k_{air}}{2R_a} \left(\frac{2u_{air} R_a}{v_{air}} \right)^{0.57}, \tag{25}$$

where k_{air}, v_{air}, and u_{air} denote the thermal conductivity, kinematic viscosity, and flow rate of air, respectively; the R_a denotes the average radius of the axle box.

3. Heat radiation:

In addition to heat conduction and convection, heat radiation could exist between the surfaces of the separation components. This conforms to Stephen–Boltzmann's law [39], and the heat radiation coefficient, E_b, is given by

$$Q_E = 5.73\sigma A_E \left[\left(\frac{T_{d1} + 273}{100} \right)^4 - \left(\frac{T_{d2} + 273}{100} \right)^4 \right], \tag{26}$$

where σ is the Stephen–Boltzmann's constant [40], A_E is the heat transfer area, and T_{d1} and T_{d2} denote the absolute temperatures of detached bodies.

3. Experimental Tests

To verify the ABB thermal model, field experiments were performed on 8 cars of high-speed trains. During the train operations from morning to night, the ABB temperature, ambient temperature, and vehicle speed are measured in real time. In one car, the location distribution of the temperature-monitoring points (ABB1–ABB4) for four ABBs of one bogie is displayed in Figure 7a. Figure 7b shows the recorded temperature variation for eight ABBs on two bogies of one car on one day. At the start-up stage of the train, the temperature of the ABBs rises as the speed increases. Subsequently, the vehicle speed fluctuates at ca. 300 km/h; also, the ABB temperature remains stable, forming a steady-state temperature band (highlighted by the gray shadow in Figure 7b). The lowest and highest temperatures of the steady-state range are 51 °C and 66 °C, respectively.
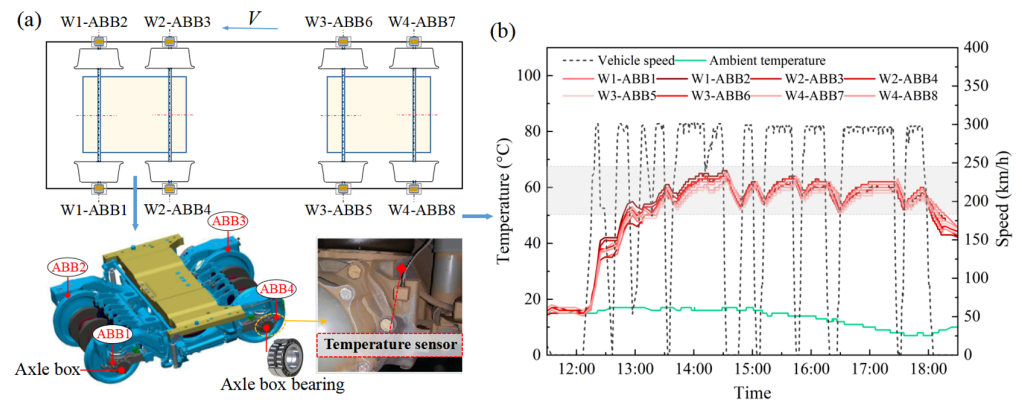

Figure 7. Field experiment: (**a**) location distribution of temperature sensors on bogies, (**b**) time history of ambient temperature, ABB temperature, and vehicle speed.

By summarizing the measured data of all ABBs on 8 cars over multiple days, the differences in steady-state temperature bands at two different vehicle speeds and under two ambient temperatures are shown in Figure 8. At V = 300 km/h, due to the increased interactions, the temperature of the ABBs is generally higher than that of the ABBs at V = 200 km/h (Figure 8a). In addition, the higher the ambient temperature, the higher the temperatures of the ABBs (Figure 8b).
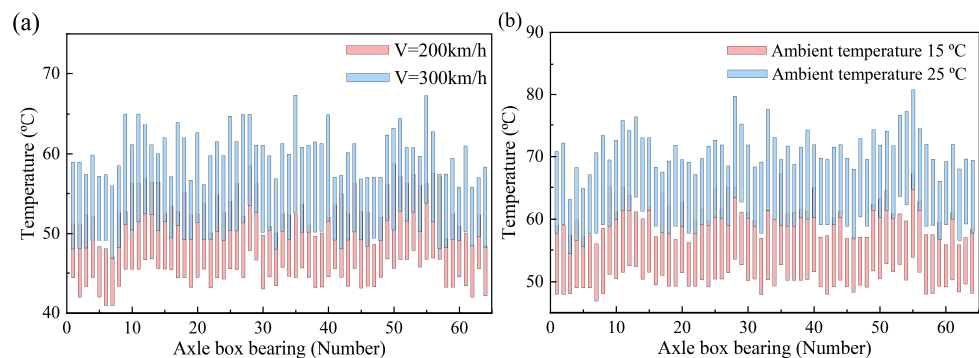

Figure 8. The measured temperature of ABB under a (**a**) speed of 200 km/h vs. 300 km/h and (**b**) ambient temperature of 15 °C vs. 25 °C.

Under the experimental conditions mentioned above, the steady-state temperatures of the ABBs are simulated by the established thermal model. Table 1 shows the simulated and experimental results of ABB temperatures under four cases with ambient temperatures of 15 and 25 °C, and vehicle speeds of 200 and 300 km/h. From Table 1, the simulation values in different conditions are all within the steady-state temperature range of the measured

data. In contrast, the maximum difference between the simulated temperature and the average experimental temperature of the ABB is ca. 2.4 °C, which is within the acceptable range in engineering. The result indicates that the proposed model can accurately and reliably estimate the temperature characteristics of ABB.

Table 1. The comparison between measured data and simulated results.

Condition	Vehicle Speed (km/h)	Ambient Temp. (°C)	Measured Temp. (°C)	Simulated Temp. (°C)
case 1	200	~15	44.64–53.08	47.62
case 2	300	~25	50.08–60.43	52.84
case 3	200	~15	53.83–64.73	58.93
case 4	300	~25	59.57–71.39	63.76

4. Temperature Characteristics of ABB

Using the proposed model, the temperature characteristics of ABBs excited by the wheel flat are investigated. Considering the almost symmetrical structure of the ABB and the discontinuities of the components (e.g., outer ring, roller, inner ring, cage, and axle box), 40 nodes in the axial and radial directions on the vertical section were selected as observation objects to analyze the temperature variations in each component of the ABB. The distribution of each node and its name are shown in Figure 9 and Table 2.
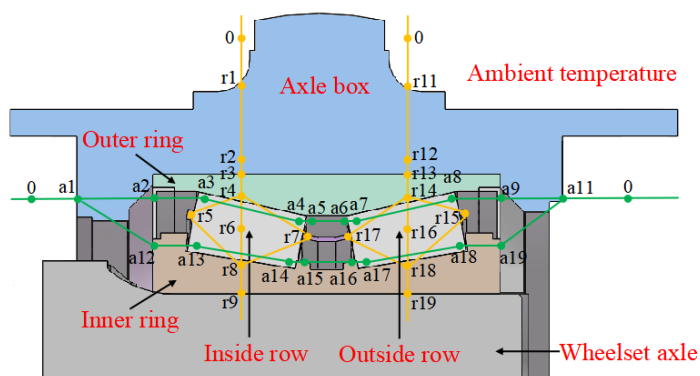

Figure 9. Axial node and radial node distribution of ABB model (0: Ambient air).

Table 2. Temperature nodes of ABB model.

Node	Description	Node	Description
Axial nodes			
a1	External surface of axle box (i)	a11	External surface of axle box (o)
a2	Outer ring end face (i)	a12	Inner ring end face (i)
a3	Roller large end–outer ring contacts (i)	a13	Roller large end–inner ring contacts (i)
a4	Roller small end–outer ring contacts (i)	a14	Roller small end–inner ring contacts (i)
a5	Outer ring–roller contacts (i)	a15	Inner ring–roller contacts (i)
a6	Outer ring–roller contacts (o)	a16	Inner ring–roller contacts (o)
a7	Roller small end–outer ring contacts (o)	a17	Roller small end–inner ring contacts (o)
a8	Roller large end–outer ring contacts (o)	a18	Roller large end–inner ring contacts (o)
a9	Outer ring end face (o)	a19	Inner ring end face (o)

Node	Description	Node	Description
Radial nodes			
r1	External surface of axle box (i)	r11	External surface of axle box (o)
r2	Internal surface of axle box (i)	r12	Internal surface of axle box (o)
r3	Axle box–outer ring contacts (i)	r13	Axle box–outer ring contacts (o)
r4	Outer ring (i)	r14	Outer ring (o)
r5	Roller large end–cage contacts (i)	r15	Roller large end–cage contacts (o)
r6	Roller (i)	r16	Roller (o)
r7	Roller small end–cage contacts (i)	r17	Roller small end–cage contacts (o)
r8	Inner ring (i)	r18	Inner ring (o)
r9	Inner ring–wheelset axle contacts (i)	r19	Inner ring–wheelset axle contacts (o)

i: Inside row; o: Outside row.

4.1. Temperature Distribution of ABB Under Normal Condition

Using the thermal analysis model of ABB established in Section 2.2 (Figure 5), the temperature distribution of the ABB is simulated in Ansys Workbench software. Based on this, the temperature fields of ABB components at V = 300 km/h are obtained (Figure 10). The overall temperature distribution of ABB exhibits 1/21 periodic symmetry along the radial direction. As shown in Figure 10b, the roller temperature is the highest, followed by the cage and inner ring temperatures, while the lowest temperature appears at the axle box. Until it transfers to the axle box, the temperature drops significantly (Figure 10a). As shown in Figure 10c,d,f, the highest temperatures occur in the contact surfaces between the rollers and ring raceways, where friction heat is generated. Subsequently, the generated heat yields a temperature increase in the roller, cage, inner ring, and outer ring via heat conduction. Under this condition, the temperature of the outer ring is lower than the inner ring temperature (Figure 10c,f); the root cause is that the external surface of the outer ring is directly connected to the internal surface of the axle box, allowing heat dissipation quickly via conduction in the axle box. Concurrently, the temperature of the roller gradually decreases from the contact area with the inner ring to the contact area with the outer ring. In detail, the higher temperature of the roller at the small end (Figure 10d) is because the region between the two rows of rollers is almost enclosed, where the generated heat is not easily transferred. In addition, the cage temperature distribution (Figure 10e) is similar to that of the roller. Considering that the cage mainly serves as a guide for the roller to revolve, its contact with rollers is continuous. Based on the results analyzed above, we can find that an excessive temperature increase significantly affects the roller of ABB, particularly at the small ends, which should be given more attention in temperature monitoring and ABB maintenance.
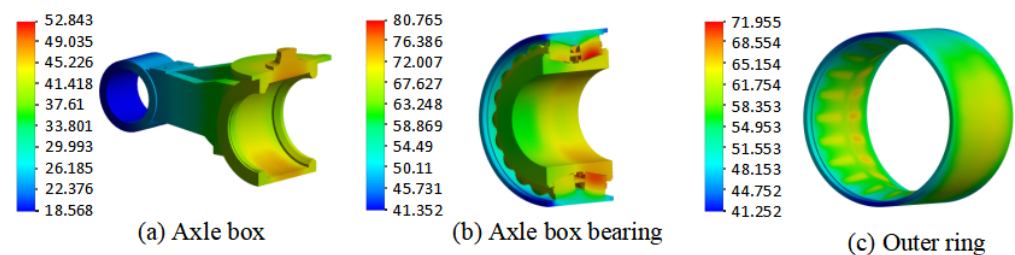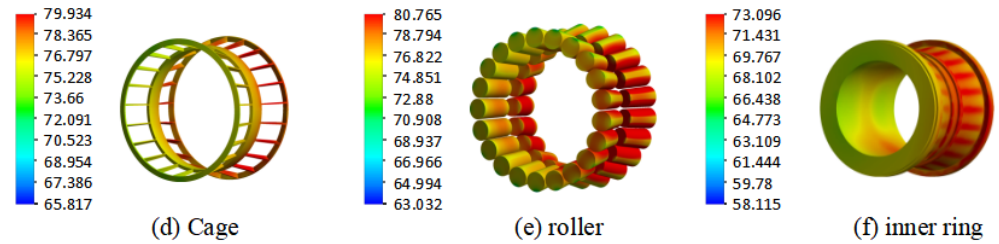

(a) Axle box (b) Axle box bearing (c) Outer ring

Figure 10. *Cont.*

Figure 10. The temperature field of (**a**) axle box, (**b**) ABB, (**c**) outer ring, (**d**) cage, (**e**) roller, and (**f**) inner ring under normal conditions (*V* = 300 km/h).

4.2. Temperature Characteristics of ABBs at Different Wheel Flat Lengths

When the defect of the wheel flat exists, the internal friction of ABB increases due to the intensified wheel–rail impact, which further induces bearing temperature variations. Comparing the temperatures for each ABB component (Figure 11a), the temperature is significantly greater in the existence of wheel flat (30 and 60 mm in length) than in its absence (0 mm long). With the wheel flat defects, the rail periodically makes contact with a wheel flat defect during vehicle operation; in this process, an obviously greater wheel–rail impact, which induces violent friction inside ABB fixed on the wheelset axle, is generated, and therefore, excessive friction heat is generated; thus, the ABB temperature increases significantly. The temperature at the outside row (o) is greater than that at the inside row (i), attributable to the intensified friction between the outside row of the roller and raceway that induces greater power loss under wheel flat excitation. Under wheel flat excitation inside ABB, the roller and cage temperatures are higher than those of the other components. Specifically, the temperature at each thermal node of the roller and cage at a flat length of 30 mm is shown in Figure 11b. For the outside row roller, the temperature of the small end (nodes a7 and a17) is slightly higher than that of the large end (nodes a8 and a18) by ~2.43 °C. The temperature distribution of the inside row of ABB excited by the wheel flat is similar to those of the outside row.
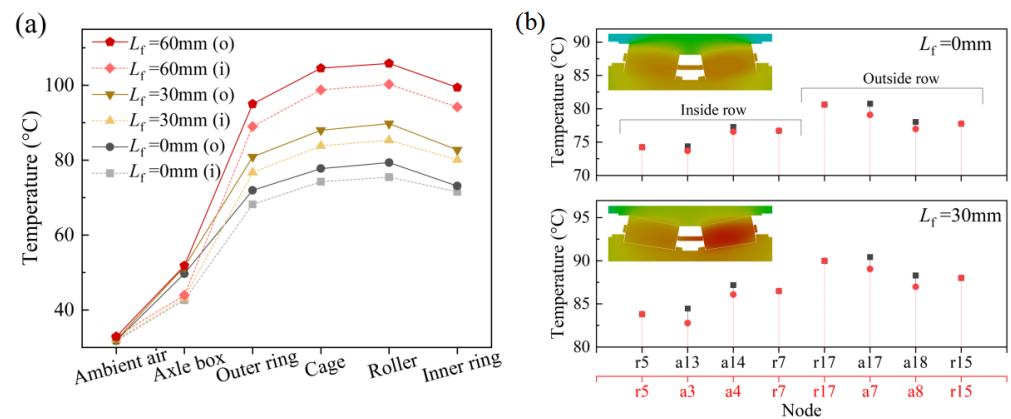

Figure 11. (**a**) Temperatures at outside row (o) and inside row (i) of ABB with L_f = 0, 30, 60 mm; (**b**) temperature at thermal nodes of bearing roller with L_f = 0 and 30 mm (*V* = 300 km/h).

Figure 12 further displays the effect of the wheel flat on ABB temperature characteristics, with the length range of 0–60 mm. Longer wheel flats, particularly $L_f \geq 30$ mm, yield a higher ABB temperature rise. When the flat length is increased from 30 to 60 mm, the temperatures of the roller's large end (nodes a13 and a18) and small end (nodes a14 and a17) are increased by ~15.60 °C and ~16.84 °C on average, and the temperature of the cage (nodes r5 and r15) is increased by ~15.74 °C on average. In addition, the temperatures of the axle box (nodes a1 and a11), outer ring (nodes r4 and r14), and inner ring (nodes r8 and r18) are increased by 1.02 °C, 13.23 °C, and 15.38 °C, respectively. This is because longer

flat excitation causes severe wheel–rail impact, which induces more violent friction and generates considerable heat, resulting in an excessive temperature increase.
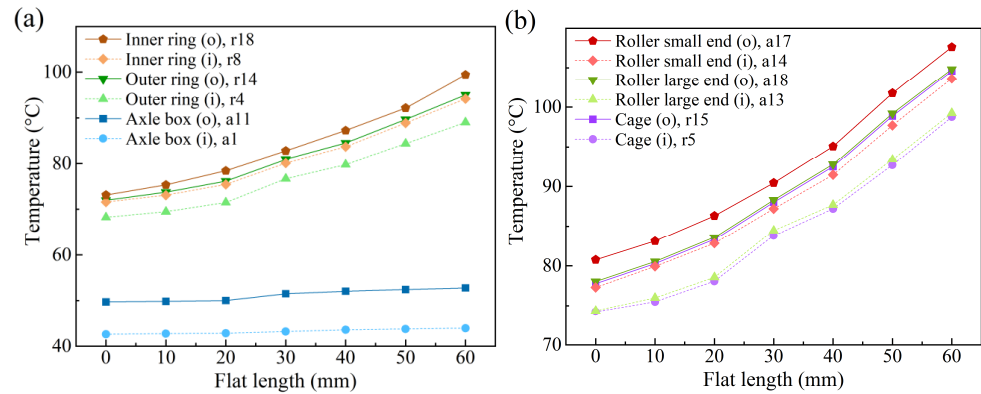

Figure 12. Temperatures of (**a**) axle box, outer ring, and inner ring, and (**b**) roller and cage, with different wheel flat lengths (V = 300 km/h).

4.3. Temperature Characteristics of ABB at Different Speeds

At different vehicle running speeds, the ABB at the end of the wheel axle continuously rotates, generating a large amount of friction heat. Particularly, as the running speed of the train continuously increases, the ABB temperature increases more significantly. Typically, slow-speed trains (50 and 150 km/h) and high-speed trains (300 and 350 km/h) were selected for the comparative analysis of the temperature characteristics of ABBs with wheel flat excitation (L_f = 30 mm; Figure 13). For slow-speed trains (Figure 13a), the temperature of the various ABB components differs slightly. For high-speed trains (Figure 13b), the temperature of each component increases significantly and differs for various components, attributable to two sources: one is the increased speed, yielding a larger amount of rolling friction power loss; the other is the larger viscous drag loss, which increases the temperature. In contrast, within the high-speed range, the ABB temperature is obviously higher. With the speed increases from 300 to 350 km/h, the temperatures of the axle box, outer ring, cage, roller, and inner ring under wheel flat excitation increase by 3.75 °C, 8.59 °C, 10.38 °C, 11.25 °C, and 9.27 °C, respectively. These results indicate that the temperature rise in the roller, cage, inner ring, outer ring, and axle box decreases in order. For the bearing roller, the temperature rises by 42.51% as the speed is enhanced from 150 to 300 km/h. In conclusion, the ABB temperature increases as the vehicle speed increases within the observation range.
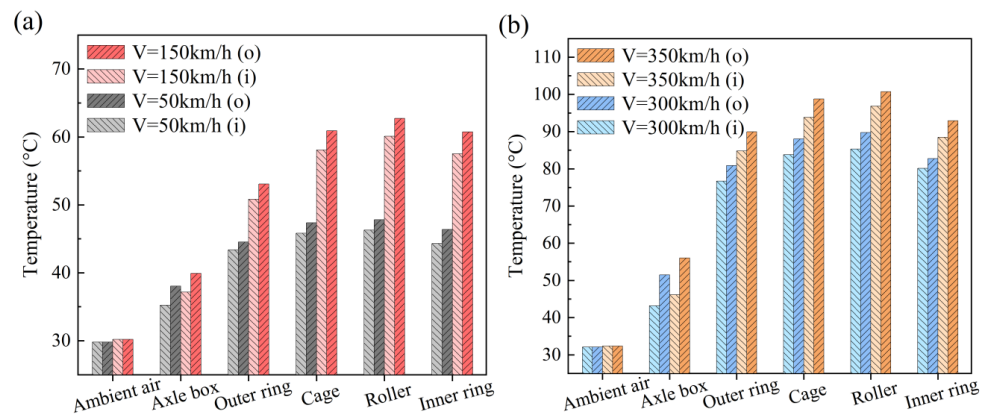

Figure 13. Temperature of components inside ABBs under (**a**) slow speed and (**b**) high speed (L_f = 30 mm).

5. Conclusions

To investigate the temperature rise in ABB under wheel flat excitation, an ABB thermal model coupling the vehicle operation environment is developed. The coupling dynamic effects between the wheel–rail force and internal ABB force as well as the elastic deformation impact of flexible axle boxes are considered. The heat conduction, convection, and radiation between the various ABB components are integrated into the model according to the actual conditions. The accuracy of the improved model is then confirmed by comparing the monitoring temperature value of an online train and the simulated results. Further, adopting the verified model, the temperature characteristics of ABBs excited by wheel flats are investigated. The main achievements are as follows:

- Longer wheel flats yield a higher temperature rise inside ABB. In particular, the temperature of the ABB outside row is greater than the ABB inside row. ABB temperature increases more significantly at higher speeds than at lower speeds.
- With wheel flat excitation, the temperature within ABB components follows the descending order of roller > cage > inner ring > outer ring > axle box. For the roller with the highest temperature, the temperature distribution gradually decreases from the contact area with the inner ring to that with the outer ring. The temperature at the small end is greater than that at the large end.

Moreover, the systematic analyses of ABB temperature characteristics under complex external excitations, e.g., track irregularity, wheel polygon, and rail defects, can be further studied in subsequent work. Bearing alignment may contribute to the heat distribution to some extent, which could also be a novel focus for future research.

Author Contributions: Conceptualization, Y.L.; methodology, Y.L.; software, Y.L. and C.Y.; validation, Y.L. and Z.W.; investigation, F.Z. and Z.W.; writing—original draft preparation, Y.L.; writing—review and editing, F.Z., F.G. and Z.W.; supervision, F.Z.; funding acquisition, W.Z. and Z.W. All authors have read and agreed to the published version of the manuscript.

Data Availability Statement: Data are contained within the article.

Conflicts of Interest: The authors declare no conflicts of interest.

References

1. Tarawneh, C.; Aranda, J.; Hernandez, V.; Crown, S.; Montalvo, J. An investigation into wayside hot-box detector efficacy and optimization. *Int. J. Rail Transp.* **2020**, *8*, 264–268. [CrossRef]
2. Mu, J.; Zeng, J.; Wang, Q.; Sang, H. Determination of mapping relation between wheel flat and wheel/rail contact force for railway freight wagon using dynamic simulation. *Proc. Inst. Mech. Eng. Part F J. Rail Rapid Transit.* **2022**, *236*, 545–556. [CrossRef]
3. Nikas, G.K. An advanced model to study the possible thermomechanical damage of lubricated sliding-rolling line contacts from soft particles. *J. Tribol.* **2001**, *123*, 828–841. [CrossRef]
4. Sun, Q.G.; Wang, Y.F.; Wang, Y.; Lv, H.B. Comparing of temperatures of rolling bearing under the oil-air lubrication to the spray lubrication. *Appl. Mech. Mater.* **2013**, *395*, 763–768. [CrossRef]
5. Hamraoui, M. Thermal behaviour of rollers during the rolling process. *Appl. Therm. Eng.* **2019**, *29*, 2386–2390. [CrossRef]
6. Wang, H.; Conry, T.; Cusano, C. Stack-up forces for normal and abnormal operating conditions in a railroad roller bearing assembly. *J. Mech. Des.* **1998**, *120*, 707–713. [CrossRef]
7. Ai, S.; Wang, W.; Wang, Y.; Zhao, Z. Temperature rise of double-row tapered roller bearings analyzed with the thermal network method. *Tribol. Int.* **2015**, *87*, 11–22. [CrossRef]
8. Li, X.; Lv, Y.; Yan, K.; Liu, J.; Hong, J. Study on the influence of thermal characteristics of rolling bearings and spindle resulted in condition of improper assembly. *Appl. Therm. Eng.* **2017**, *114*, 221–233. [CrossRef]

9. Yan, K.; Wang, N.; Zhai, Q.; Zhu, Y.; Zhang, J.; Niu, Q. Theoretical and experimental investigation on the thermal characteristics of double-row tapered roller bearings of high speed locomotive. *Int. J. Heat Mass Transf.* **2015**, *84*, 1119–1130. [CrossRef]

10. Tarawneh, C.M.; Cole, K.D.; Wilson, B.M.; Alnaimat, F. Experiments and models for the thermal response of railroad tapered-roller bearings. *Int. J. Heat Mass Tranf.* **2008**, *51*, 5794–5803. [CrossRef]

11. Cole, K.D.; Tarawneh, C.M.; Fuentes, A.A.; Wilson, B.; Navarro, L. Thermal models of railroad wheels and bearings. *Int. J. Heat Mass Tranf.* **2010**, *53*, 1636–1645. [CrossRef]

12. Tarawneh, C.M.; Fuentes, A.A.; Kypuros, J.A.; Navarro, L.A.; Vaipan, A.G.; Wilson, B.M. Thermal modeling of a railroad tapered-roller bearing using finite element analysis. *J. Therm. Sci. Eng. Appl.* **2012**, *4*, 031002. [CrossRef]

13. Blanuša, V.; Zeljković, M.; Milisavlevich, B.M.; Savić, B. Mathematical modelling of thermal behaviour of cylindrical roller bearing for towed railway vehicles. *Teh. Vjesn.* **2017**, *24*, 211–217.

14. Zhou, X.; Zhu, Q.; Wen, B.; Zhao, G.; Han, Q. Experimental investigation on temperature field of a double-row tapered roller bearing. *Tribol. Trans.* **2019**, *62*, 1086–1098. [CrossRef]

15. Gao, P.; Tang, W.; Cui, Y.; Wang, Y.; Mo, G.; Yin, J. Theoretical and experimental investigation on thermal characteristics of railway double-row tapered roller bearing. *Energies* **2022**, *15*, 4217. [CrossRef]

16. Wang, Z.; Cheng, Y.; Allen, P.; Yin, Z.; Zou, D.; Zhang, W. Analysis of vibration and temperature on the axle box bearing of a high-speed train. *Veh. Syst. Dyn.* **2019**, *58*, 1605–1628. [CrossRef]

17. Luo, Y.; Zhang, F.; Wang, Z.; Zhang, W.; Wang, Y.; Liu, L. Dynamic response of the axle-box bearing of a high-speed train excited by wheel flat. *Veh. Syst. Dyn.* **2024**, *62*, 2260–2282. [CrossRef]

18. Zander, M.; Otto, M.; Lohner, T.; Stahl, K. Evaluation of friction calculation methods for rolling bearings. *Forsch. Ingenieurwes.* **2023**, *87*, 1307–1316. [CrossRef]

19. Wu, X.; Rakheja, S.; Ahmed, A.; Chi, M. Influence of a flexible wheelset on the dynamic responses of a high-speed railway car due to a wheel flat. *Proc. Inst. Mech. Eng. Part F J. Rail Rapid Transit.* **2018**, *232*, 1033–1048. [CrossRef]

20. Wang, Z.; Cheng, Y.; Mei, G.; Zhang, W.; Huang, G.; Yin, Z. Torsional vibration analysis of the gear transmission system of high-speed trains with wheel defects. *Proc. Inst. Mech. Eng. Part F J. Rail Rapid Transit.* **2020**, *234*, 123–133. [CrossRef]

21. Zhai, W.; Xia, H.; Cai, C.; Gao, M.; Li, X.; Guo, X.; Zhang, N.; Wang, K. High-speed train–track–bridge dynamic interactions–Part I: Theoretical model and numerical simulation. *Int. J. Rail Transp.* **2013**, *1*, 3–24. [CrossRef]

22. Zhai, W.; Sun, X. A detailed model for investigating vertical interaction between railway vehicle and track. *Veh. Syst. Dyn.* **1994**, *23*, 603–615. [CrossRef]

23. Shen, Z.; Hedrick, J.; Elkins, J. A comparison of alternative creep force models for rail vehicle dynamic analysis. *Veh. Syst. Dyn.* **1983**, *12*, 79–83. [CrossRef]

24. Kalker, J.J. *Three-Dimensional Elastic Bodies in Rolling Contact*; Springer Science & Business Media: Berlin/Heidelberg, Germany, 2013.

25. Zhai, Z.; Zhu, S.; Yuan, X.; He, Z.; Cai, C. Nonlinear effects of a new mesh-type rail pad on the coupled vehicle-slab track dynamics system under extremely cold environment. *Proc. Inst. Mech. Eng. Part F J. Rail Rapid Transit.* **2023**, *237*, 285–296. [CrossRef]

26. Hou, K.; Kalousek, J.; Dong, R. A dynamic model for an asymmetrical vehicle/track system. *J. Sound Vib.* **2003**, *267*, 591–604. [CrossRef]

27. Wang, Z.; Cheng, Y.; Yang, B.; Xiao, S.; Zhang, W. Raceway defect features of a high-speed train axle box bearing in the vehicle–track coupled system. *IEEE Trans. Instrum. Meas.* **2022**, *72*, 3503615. [CrossRef]

28. Liu, Y.; Chen, Z.; Zhai, W.; Wang, K. Dynamic investigation of traction motor bearing in a locomotive under excitation from track random geometry irregularity. *Int. J. Rail Transp.* **2022**, *10*, 72–94. [CrossRef]

29. Wu, P.; He, C.; Chang, Z.; Li, X.; Ren, Z.; Li, D.; Ren, C. Theoretical calculation models and measurement of friction torque for rolling bearings: State of the art. *J. Braz. Soc. Mech. Sci.* **2022**, *44*, 435. [CrossRef]

30. Pinheiro, K.A.; Filho, S.D.S.C.; Vaz, J.R.P.; Mesquita, A.L.A. Effect of bearing dissipative torques on the dynamic behavior of H-Darrieus wind turbines. *J. Braz. Soc. Mech. Sci.* **2021**, *43*, 410. [CrossRef]

31. Liu, J.; Yan, Z.; Shao, Y. An investigation for the friction torque of a needle roller bearing with the roundness error. *Mech. Mach. Theory* **2018**, *121*, 259–272. [CrossRef]

32. Kanazawa, Y.; De Laurentis, N.; Kadiric, A. Studies of friction in grease-lubricated rolling bearings using ball-on-disc and full bearing tests. *Tribol. Trans.* **2020**, *63*, 77–89. [CrossRef]

33. Bălan, M.R.D.; Stamate, V.C.; Houpert, L.; Olaru, D.N. The influence of the lubricant viscosity on the rolling friction torque. *Tribol. Int.* **2024**, *72*, 1–12. [CrossRef]

34. Goncalves, D.; Cousseau, T.; Gama, A.; Campos, A.V.; Seabra, J.H. Friction torque in thrust roller bearings lubricated with greases, their base oils and bleed-oils. *Tribol. Int.* **2017**, *107*, 306–319. [CrossRef]

35. Vaz, J.R.; Wood, D.H.; Bhattacharjee, D.; Lins, E.F. Drivetrain resistance and starting performance of a small wind turbine. *Renew. Energy* **2018**, *117*, 509–519. [CrossRef]

36. Brändlein, J. *Ball and Roller Bearings: Theory, Design and Application*; Wiley: Hoboken, NJ, USA, 1999.

37. Burton, R.A.; Staph, H. Thermally activated seizure of angular contact bearings. *ASLE Trans.* **1967**, *10*, 408–417. [CrossRef]

38. Pouly, F.; Changenet, C.; Ville, F.; Velex, P.; Damiens, B. Investigations on the power losses and thermal behaviour of rolling element bearings. *Proc. Inst. Mech. Eng. Part J-J. Eng.* **2010**, *224*, 925–933. [CrossRef]

39. Harris, T.A.; Kotzalas, M.N. *Advanced Concepts of Bearing Technology: Rolling Bearing Analysis*; CRC Press: Boca Raton, FL, USA, 2006.

40. Zhang, L.; Wang, Z.; Wang, Q.; Mo, J.; Feng, J.; Wang, K. The effect of wheel polygonal wear on temperature and vibration characteristics of a high-speed train braking system. *Mech. Syst. Signal Process.* **2023**, *186*, 109864. [CrossRef]